

Regions of Interest Segmentation from LiDAR Point Cloud for Multirotor Aerial Vehicles

Geesara Kulathunga¹, Roman Fedorenko¹, Alexandr Klimchik¹

Abstract—We propose a novel filter for segmenting the regions of interest from LiDAR 3D point cloud for multirotor aerial vehicles. It is specially targeted for real-time applications and works on sparse LiDAR point clouds without preliminary mapping. We use this filter as a crucial component of fast obstacle avoidance system for agriculture drone operating at low altitude. As the first step, each point cloud is transformed into a depth image and then identify places near to the vehicle (local maxima) by locating areas with high pixel densities. Afterwards, we merge the original depth image with identified locations after maximizing intensities of pixels in which local maxima were obtained. Next step is to calculate the range angle image that represents angles between two consecutive laser beams based on the improved depth image. Once the corresponding range angle image is constructed, smoothing is applied to reduce the noise. This allows separating the regions of interest. The filter has been tested on various simulated environments as well as an actual drone and provides real-time performance. We make our source code, dataset² and real world experiment³ available online.

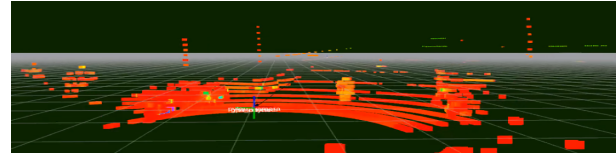
I. INTRODUCTION

Over the past two decades, LiDAR technology has been utilized in autonomous vehicles extensively addressing various problems including Multi-Target Tracking (MTT) [1], road and road-edge detection [2], pedestrian recognition and tracking [3], etc. On the other hand, mass produced Multirotor Aerial Vehicles (MAVs) were not able to apply LiDAR based technologies due to the various limitations such as computational complexity, maximum weight limit and power constrain for longer flight duration. Nevertheless, advancements of the advanced MAVs and faster growth of computational capabilities (e.g., processors, random access memory (RAM), etc.) for executing a large number of instructions per cycle and producing lightweight batteries with high power density, most of the LiDAR technologies and complex algorithms can be executed on board up to some extent. After starting LiDAR as a one of the main sources of visionary sensor, it opens a new paradigm for robust planning and navigation based applications which helps to accomplish different tasks such as surveillance and transportation. The recent work of B. Zhou [4] and S. Liu [5]

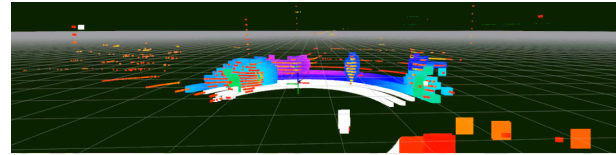
¹ Center for Technologies in Robotics and Mechatronics Components, Innopolis University, Russia
ggesara@gmail.com, r.fedorenko@innopolis.ru, a.klimchik@innopolis.ru

²Source code and dataset are available at <https://github.com/GPrathap/hagen.git>

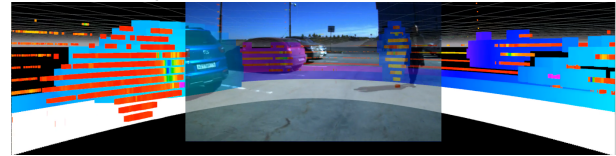
³Real-world experiment result can be found on the following link: https://www.youtube.com/watch?v=iHd_ZkhKPjC



(a) Raw point cloud from Velodyne-16 LiDAR



(b) White color represents the regions of uninterest and the other colors depict regions of interest on the point cloud which is shown in Fig 1a



(c) The camera projection on point cloud with the proposed filter result

Fig. 1: The proposed filter results

propose a quadrotors motion planning system for fast flight in 3-D complex environments only using LiDAR, i.e., visionary sensor.

In this work, we propose a new filter called “Hagen” for separating regions of interest which specially targeted real-time based applications for MAVs. Thus, it avoids building incremental map that is computationally expensive of the environment. Instead, it uses a set of consecutive point clouds and concatenates them in a sliding window fashion. Afterwards, the concatenated point cloud is utilized for further processing. The proposed filter is designed in a way that it starts detecting objects that are closer to the MAV from the top level to the bottom level of LiDAR laser beams. This feature could use with a path planner, not let MAV to fly into a trap where there is no direction to come out unless it cloud not find the reverse direction. If LiDAR is only the sensor that applied for reasoning of the environment, search space of the LiDAR will eventually become the feasible search space of MAV. Scanning nature of LiDAR helps to start detecting objects from the top to bottom level. That will help to avoid traversing MAV into terrain or obstacles. How filter processes 3D LiDAR point clouds is shown in Fig. 1.

Our Contributions: Proposing a filter to separate regions of interest is the main contribution. Under which,

- 1) Improving depth image by finding local maxima by applying persistence homology complemented by applying modified bilateral filter for sharpening the detected local maxima
- 2) Object detection process starts off detecting objects closer to LiDAR from the top-level (laser beams)
- 3) Apply Singular Spectrum Analysis (SSA) for smoothing the range angle image and control the smoothness

II. RELATED WORK

In the work of C.Tongtong[6], ground segmentation is performed on 3D LiDAR point cloud, building a polar grid map. It applies 1D Gaussian Process (GP) regression model and Incremental Sample Consensus (INSAC) algorithm for segmentation. They have achieved good segmentation results in the different type of scenarios including urban and countryside environments. The authors of [7] present a set of segmentation of dense 3D data algorithms. Empirically they have noticed that prior ground extraction leads to an improvement of the segmentation performance. The work by M. Himmelsbach [8] shows long-range 3D point clouds segmentation in a real-time and later classification of segmented objects. To reduce the execution time and increase efficiency, their approach was split into solving of two subproblems: ground plane estimation and fast 2D connected components labelling. In our approach, it happens in the opposite direction where fast 2D connected components labelling (regions of interest) is followed by uninteresting regions separation. The ground plane also can be within the regions of interest if MAV flies closer to the ground that is the main purpose of doing this way. F. Moosmann [9] presents a fast algorithm that works with a high volume of 3D LiDAR data in a real-time. It uses a novel unified generic criterion based on local convexity measures for separation of ground and non-ground which is based on a graph data structure. The authors of [10] present an implementation of the ground detection methodology with filtration of forest points from LiDAR-based dense 3D point cloud using the Cloth Simulation Filtering (CSF) algorithm. The methodology requires dense mapping and offline analysis but allows to recover a terrestrial relief and create a landscape map of a forestry region.

Most of the 3D point cloud segmentation techniques over the last decade were based on an either statistical or probabilistic model. But B. Wu [11] proposes a novel approach for semantic segmentation of road-objects from 3D LiDAR point clouds based on neural networks. They have formulated the problem as a point-wise classification problem using a convolutional neural network (CNN). A transformed LiDAR point cloud is taken as the input for the model. Point-wise label map or cluster will be the output of the model. The recent development of hardware helps to run such high computing power demanding algorithms effectively. The authors of [12], also uses 3D CNN for detecting of small and potentially obscured obstacles in vegetated terrain incorporating volumetric occupancy map. Initially, they need to train a model what sort of terrain to be detected from raw occupancy data.

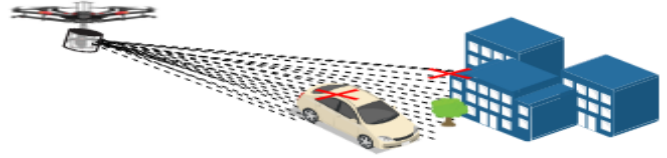


Fig. 2: Illustration of the superposition of objects between close, i.e., part of the car and far, i.e., tree and part of the building whose distance or depth from LiDAR will be in the same neighborhood region of the depth image. Nearest points in the point cloud from LiDAR are marked with the red crosses

Filtering is one of the most fundamental techniques of computer vision. For example, a Gaussian filter computes the weighted average around the given pixel location with a given size of a kernel. Bilateral filter also uses a somewhat similar approach but preserving edges around each considered pixel. In this work[13], formulate obtaining dense depth-map using local spatial interpolation that depends on sliding window-based approach in which BF is employed. They have modified conventional BF to achieve proper upsampling which can preserve foreground-background discontinuities. In that way they were able to acquire high resolution depth-maps by upsampling of 3D-LiDAR data. In this research, Bilateral Filter (BF) is applied to sharpen locations around local maxima detected as shown in Fig. 3.

Usually, appropriate smoothing is applied on the filtered output to improve the robustness. The main intuition of smoothing a signal is to construct an approximate signal which tries to capture meaningful patterns while leaving out noise or other rapid phenomena. SSA is one of the smoothing techniques which gives a highly accurate and concise result. SSA is utilized extensively in the biomedical related application for smoothing signals and find some hidden patterns within it (e.g., [14], [15] and [16]).

III. SEPARATING REGIONS OF INTEREST

Typically, ground plane can be separated simply removing points that are lower than the location of the LiDAR (assume that installed location is known) or RANSAC-based plane fitting. However, none of those methods does work for MAVs because MAV altitude can change anytime in contrast to ground vehicles. Hence, ground plane also can be considered within the regions of interest if it flies closer to the ground. The main steps of the proposed filter is provided in Algorithm. 1. Inputs for the filter: *point_cloud*, *ground_removal_angle* (explain in Sec. III-C), *number_of_principal_components* and *smoothing_window_size* (explain in Sec. III-D).

A. Depth Image Estimation from Point Cloud

We used Velodyne VLP16 LiDAR for our experiments, however the proposed algorithm could be used with other LiDARs (e.g, Velodyne HDL-64E, HDL-32E, etc). VLP16

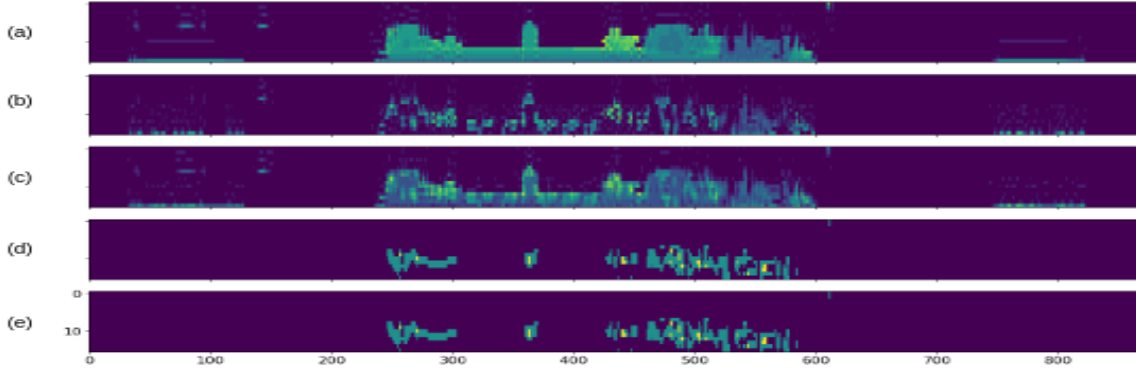


Fig. 3: (a) depicts the depth image ($depth_img$) which is transformed from a point cloud (corresponds to point cloud shown in Fig. 1a). The result of local maxima detection ($filtered_img$) is shown in (b). Mean image ($processed_img$) is shown in (c). Range angle image $angle_img$ and smoothed range angled image ($smoothed_angle_img$) are shown in (d) and (e) respectively

Algorithm 1 Separation of regions of interest

Input $point_cloud$, $number_of_principle_components$ (PC), $ground_removal_angle$ (β), $smoothing_window_size$ (W)

Output $region_of_interest$, $non_region_of_interest$

- 1: $depth_img \leftarrow ConstructDepthImage()$
 - 2: $filtered_img \leftarrow ApplyLocalMaxima2DFinder()$
 - 3: $processed_depth_img \leftarrow (depth_img + filtered_img)/2$
 - 4: $angle_img \leftarrow ConstructAngleImage()$
 - 5: $smoothed_angle_img \leftarrow ApplySSASmoothing()$
 - 6: $roi, non_roi \leftarrow LabelRegionOfInterest()$
-

provides the point cloud which consists of 16 laser beams that covers ± 15 degrees vertically and 360 degrees horizontally. Processing point cloud itself is time-consuming which is not suited for real-time analysis. Thus, we have decided to reduce space dimension 3D to 2D where disparity map or depth map is employed for separation of the regions of interest. Width of the depth image is set for 870 (I_w). 870 is selected empirically under which horizontal resolution becomes $0.413(360/870)$ degrees/pixel. It can be changed, but it may affect the performance and the accuracy. Depth image height (I_h) is set for 16 because VLP16 LiDAR has only 16 channels. To transform a point cloud into a depth image, each point in the point cloud to be assigned to a pixel in the depth image. Distance or depth to each considered point corresponds to an intensity of the chosen pixel. If there are multiple points corresponded to the same pixel location, we keep the closest distance from the LiDAR. Once non-ground is separated in 2D space, it is needed to acquire the corresponding points in the point cloud from the depth image. Thus, while estimating the depth image, we keep a record which points belongs to which pixel location. This mapper is named the $depth_mapper$ which will be using in the following sections.

Following steps are required to create the depth image:

- 1) Let $(x_i, y_i, z_i : i = 1, \dots, N)$ are the points in a cloud, where N is the number of points
- 2) Estimate angles on x and y directions for a given point:

$$angle_x_i = \text{asin}\left(\frac{z_i}{dist_i}\right), \quad angle_y_i = \text{atan2}(y_i, x_i) \quad (1)$$

- 3) 360 degrees are split into I_w number of pixels; 30 degrees are split into I_h number of pixels. Then we get closest matching row and column that corresponds with $angle_x$ and $angle_y$ in degrees. It will be the pixel location on the depth image. Here $dist_i = \sqrt{x_i^2 + y_i^2 + z_i^2}$ is the intensity value.

A similar idea has proposed in [17] as well. After performing this, depth image can be constructed as shown in Fig. 3a.

B. Local Maxima Detection in Depth Image

Intuition of detecting local maxima locations is shown in Fig. 2. We are interested in finding locations of high pixel intensity (local maxima) which correspond to closest objects from current pose of MAV. Extracting local maxima from given images that are in high-dimensional space is generally challenging because of incompleteness and noise. In applied mathematics, Topological Data Analysis (TDA)[18] is an approach for analyzing data by using topological properties. This allows to find some hidden structures or patterns. Persistence Homology (PH)[19] is one of the dominant mathematical tools employed for this purpose. PH provides a proper way of analysing such data while being less sensitive to a particular metric and transforming original space into different space which is robust to noise.

To get a clear intuition of how PH applies for local maxima detection, let's consider Fig. 4. Though we are interested in local maxima, some of the local maxima might be irrelevant for time to time. For example, local maxima near 155 must be considered while discarding local maxima at 165.

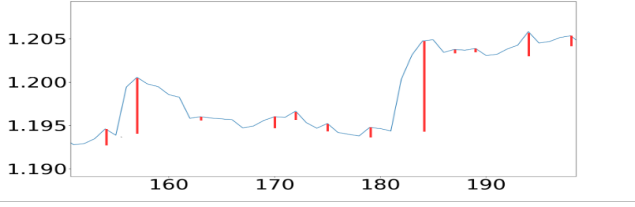


Fig. 4: Blue color curve shows how normalized pixel intensities are propagated over given row of image. Red color vertical lines represent barcode for the most significant local minima

Those false positives are arisen because of the noise of the image. Hence, false positives should be eliminated. Noise can be removed by smoothing the image. Nonetheless, this comes with a cost (e.g., some of sharpen local maxima get vanished or dampened, intensity level of pixel will change if there is no proper normalization, etc). Thus, it would be better to operate on the original data itself. In Persistent Homology, there is a concept called barcode. A barcode represents each persistent generator with a vertical line which begins at the first filtration level when it arises and ending at the second filtration level when it disappears. Persistent generator, first filtration level and second filtration level are corresponded to distance between detected local maxima to consecutive local minima, local maxima and local minima respectively. In Fig. 4, red colored lines depict the most persistent 0-dimensional cycles [20] where the local maxima have been detected. Hence, PH is employed for detecting relative maxima in noise-resilient fashion in 2D space as shown in Fig. 5.

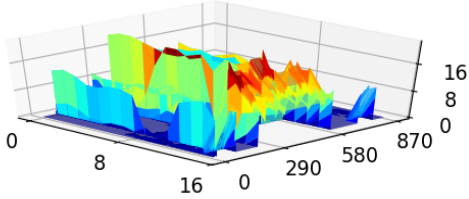


Fig. 5: Local minima detection of *depth_img* where blue color plane depicts the pixel locations of *depth_img* and strength of local maxima is varied from blue to red along the orthogonal direction to the image plane

Hence, PH finds the relative maxima in noise-resilient fashion. Once the most persistent local maxima have been detected, it is needed to sharpen those locations in depth image without affecting neighbour pixels. A bilateral filter (BF) is one of the techniques to achieve this because BF is a non-linear, edge-preserving, and noise-reducing smoothing filter. It replaces the intensity of each of the pixels with a weighted average of intensity values from nearby pixels. We have modified BF slightly different way which get more accurate result compare to the original BF [21]. The modified

BF is given as follows.

$$I^{filtered}(x) = \frac{1}{W_p} \sum_{x_i \in \Omega} I(x) G(x - x_i, \sigma_x) G(dis(x, x_i), \sigma_n) + I(x) \quad (2)$$

and normalization term, W_p is defined as

$$W_p = \sum_{x_i \in \Omega} G(x - x_i, \sigma_x) G(dis(x, x_i), \sigma_n) \quad (3)$$

$$G(\mu, \sigma) = \frac{1}{\sigma \sqrt{2\pi}} \exp^{-\frac{1}{2}(\mu/\sigma)^2}, \quad dis(x, x_i) = \sqrt{x^2 + x_i^2} \quad (4)$$

where $I^{filtered}(x)$ is the filtered image, I is the depth image, x are the coordinates of local maxima that are detected, Ω is the 8 neighbours around each x , $G(\mu, \sigma)$ is a Gaussian function where μ is the mean and σ is the standard deviation, σ_x and σ_n are the standard deviations which are constant all the time; values are set as 1.2 and 1.3 respectively which were estimated empirically. $dis(x, x_i)$ is utilized to estimate distance between x and $x_i \in \Omega$ where $i = 1, \dots, 8$.

C. Constructing Range Angle Image

In each iteration, the depth image is followed by range angle image are constructed. Since laser beams cover ± 15 degrees vertically and I_h is 16, it is needed to calculated 15 vertical angles in which each angle estimated as angle between the horizontal plane of the LiDAR and considered laser beam which varies from LiDAR to LiDAR. As shown in Fig. 6, $\epsilon_{r,c}$ and $\epsilon_{r-1,c}$ are two vertical angles that correspond to two consecutive rows with a considered column, i.e., $r-1, c$ and r, c . Thus, each range angle (α) of the range angle image is calculated considering depths (i.e., depicts in red color lines in Fig. 6) at considered consecutive rows and a column in depth image. Hence, the range angle image is constructed with 15×870 ($(I_h - 1)I_w$) resolution. Let define two consecutive laser beams that are projected on a car which are shown in red colored lines in Fig. 6. Since $\epsilon_{r,c}$ and $\epsilon_{r-1,c}$ are known, α can be calculated as follows

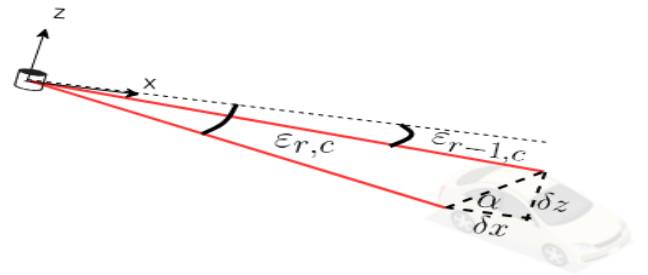


Fig. 6: Illustration of how α is calculated. To construct range angle image, $(I_h - 1)I_w$ number of α angles to be calculated as follows

$$\alpha = \text{atan2}(\delta z, \delta x),$$

$$\delta z = |D_{r-1,c} \sin(\epsilon_{r-1,c}) - D_{r,c} \sin(\epsilon_{r,c})|, \quad (5)$$

$$\delta x = |D_{r-1,c} \cos(\epsilon_{r-1,c}) - D_{r,c} \cos(\epsilon_{r,c})|$$

where $D_{r,c}$ is distance or depth at (r, c) in the depth image. As shown in Fig. 6, $\epsilon_{r,c}$ and $\epsilon_{r-1,c}$ are vertical angles in

between r and $r+1$ rows which corresponds with c -th column.
 $(r, c) = (1, \dots, I_h - 1; 0, \dots, I_w - 1)$

D. Smoothing Range Angles with SSA

SSA[22] is a powerful non-parametric spectral estimation technique for time series analysing and forecasting. SSA incorporates elements of classical time series analysis, multivariate statistics, dynamical systems and signal processing. In this work, SSA has been chosen over other smoothing techniques because of several reasons. When MAV flies closer to ground, ground plane should be considered, if not only objects closer to MAV should be considered. SSA provides this capability together with depth image based on the smoothing factor (PC). Following section explains how it is being achieved.

SSA is applied for smoothing out the range angle image in column-wise. Let define angles in each column, $\Theta = (\alpha_0, \dots, \alpha_{N-1}) \in \mathbb{R}$ of length N (I_h). The SSA algorithm consists of two main steps: decomposition of a given series and reconstruction by adding desired principal components.

1) *Decomposition*: In this stage, Θ is rearranged into $W \times K$ matrix which is called as the trajectory matrix ($X \in \mathbb{R}$). W is the window length or *smoothing_window_size* ($1 < W < N$). K can be formulated as $K = N - W + 1$. We fix the value for W as 8 even it is a configurable parameter for the filter. This assumption is due to each column consist of 16 pixels and two iterations were assumed to be enough that made empirically. Furthermore, if you are going to use 32 or 64 channel LiDAR it is better to increase W .

$$X = [X_1 : \dots : X_K], \quad X_j = [\theta_{j-1}, \dots, \theta_{j+W-2}]^T \quad (6)$$

where $j = 1, \dots, K$. Then Singular Value Decomposition (SVD) is applied on X , where j th component of SVD is specified by j th eigenvalue λ_j and eigenvector U_j of XX^T .

$$X = \sum_{j=1}^d \sqrt{\lambda_j} U_j V_j^T, \quad V_j = \frac{X^T U_j}{\sqrt{\lambda_j}} \quad (7)$$

where $d = \max\{j : \lambda_j > 0\}$. Since X is a Hankel matrix (or catalecticant matrix) and XX^T is a positive-definite matrix, their eigenvalues (λ_j) are positive as well. Then, eigenvectors of X are ordered in decreasing order of corresponding eigenvalues.

2) *Reconstruction*: In this stage, select a set of SVD components (PC) and averaging along entries (hankelization) with indices of the X from the selected components of the SVD. More about hankelization can be found in [23]. In Fig. 7, it is shown how principal components are extracted. Based on PC , smoothness will vary. If all the principal components are taken, it implies that there is no smoothing present under which ground plane can be present within the interest of regions. Thus, PC should be selected based on the area where MAV flies.

E. Connected Components Extraction with BFS

This is the last step of the proposed filter. In Algorithm. 2, it is given the procedure of the process and

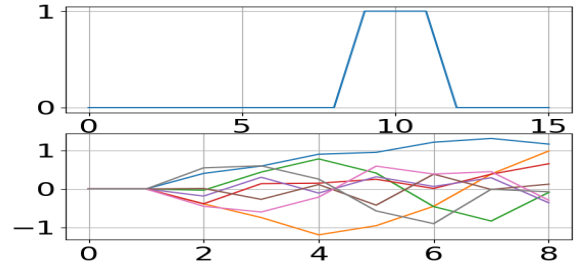


Fig. 7: Principal components extraction corresponds to 370th column of Fig. 1d. In this figure, the first subfigure depicts the intensity changes over column-wise. The second subfigure represents corresponding principal components

Algorithm 2 Connected components extraction with BFS

```

1: procedure SEPARATIONREGIONOFINTEREST()
2:   selected_depth_points  $\leftarrow$  []
3:   labeled_image  $\leftarrow$  []
4:   selected_depth_val  $\leftarrow$  Inf
5:   for  $c = 0, \dots, I_w$  do
6:     selected_depth  $\leftarrow$   $-1, -1$ 
7:     depth_is_set  $\leftarrow$  false
8:     for  $r = I_h - 1, \dots, 0$  do
9:       depth  $\leftarrow$  processed_depth_img( $r, c$ )
10:      if depth  $>$   $0.01$  & !depth_is_set then
11:        depth_is_set  $\leftarrow$  true
12:        selected_depth_points  $\leftarrow$  push( $r, c$ )
13:      end if
14:      if depth  $<$  selected_depth then
15:        selected_depth_val  $\leftarrow$  depth
16:        selected_depth  $\leftarrow$  ( $r, c$ )
17:      end if
18:    end for
19:    if selected_depth_val  $>$   $0.01$  then
20:      selected_depth_points  $\leftarrow$  pushselected_depth
21:    end if
22:  end for
23:  for depth_point : selected_depth_points do
24:    LabelConnectedComponent(depth_point,
25:      ground_removal_angle, labeled_image)
26:  end for
end procedure

```

LabelConnectedComponent() is utilized for finding connected components using the breadth-first search (BFS). The idea used was initially proposed in [24], a few modifications have been made to improve performance and accuracy. Once regions of interest are labelled, corresponding cloud points can be extracted using the *depth_mapper* (refer to the Sec. III-A). The result of this is shown in Fig. 1b.

IV. EXPERIMENTAL EVALUATION

This section mainly focuses on evaluating specific aspects of the proposed filter detailed in Sec. III and assessing the performance of the system. Since the filter is designed as a parametric model, there are three hyperparameters: PC, β and W are needed to fine tune for getting a stable result. To evaluate how those affect on the final result, initially LiDAR and filter output (point clouds) are projected on camera as shown in Fig. 1c within the camera's field of view (FOV). Thus, evaluation is done only on the region covered by camera's FOV considering as an image segmentation problem. Hence, F_1 is used as the evaluation metric which is one of the well-known widely used evaluation matrices in image segmentation applications.

$$F_1 = 2 \frac{P * R}{P + R}, P = \frac{t_p}{t_p + f_p}, R = \frac{t_r}{t_r + f_r} \quad (8)$$

where P denotes the precision, R is for recall, t_p, t_r, f_p, f_r are true positive, true negative, false positive and false negative respectively. The F_1 score is defined as the harmonic mean of P and R . In mathematics, harmonic is the most suitable tool for work with rates and ratios. Since precision and recall are ratios, it is one of the most appropriate tools for estimating the filter accuracy. As the first part

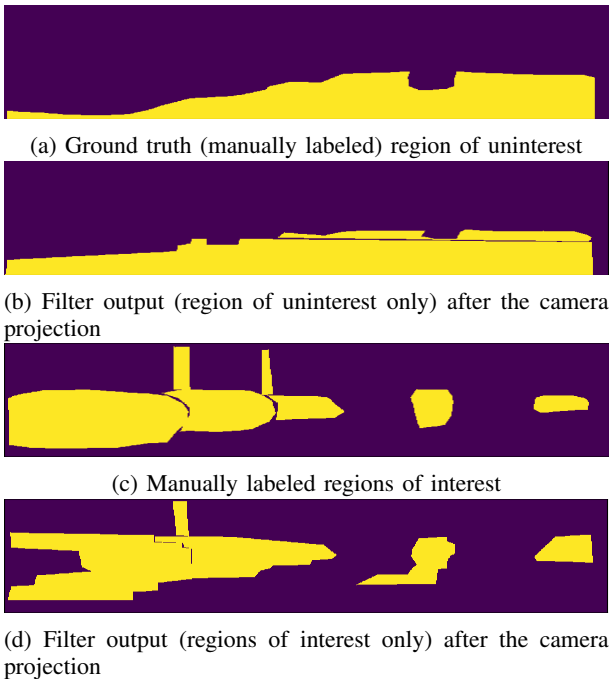


Fig. 8: Labeled images correspond with Fig. 1

of the evaluation, a set of images consisting of projected LiDAR point cloud within camera's FOV was manually selected. And we segmented them into two separate classes: regions of interest and region of uninterest as shown in Fig. 8a and Fig. 8c. Afterword, we projected filter output on camera space as regions of interest and region of uninterest separately and labelled them as shown in Fig. 8b and Fig. 8d. In this way, 50 images were labelled for the each of the

TABLE I: Changing the angle β while fixing PC (5) to evaluate how β will affect on the final accuracy of the filter

Angle β	Region of Uninterest			regions of interest		
	P	R	F1	P	R	F1
5	0.948	0.77	0.856	0.825	0.63	0.715
7.5	0.931	0.748	0.83	0.872	0.717	0.787
10	0.925	0.762	0.82	0.892	0.738	0.808
12.5	0.897	0.7	0.78	0.862	0.735	0.794

classes, overall 200 images for a given specific parameter configuration (PC, β and W). As mentioned in Sec. III-D, W is fix for this experiment. Initially, we ran the proposed filter on a set of ROS bags several times while changing PC and β values. Along with that, we came up with a hypothesis for the proper value combination of the hyperparameters, i.e., PC (5) and β (10 degrees). To claim our hypothesis was correct or wrong, PC and β were varied around the observed values. Table I and Table II show how those affect the final result of the proposed filter.

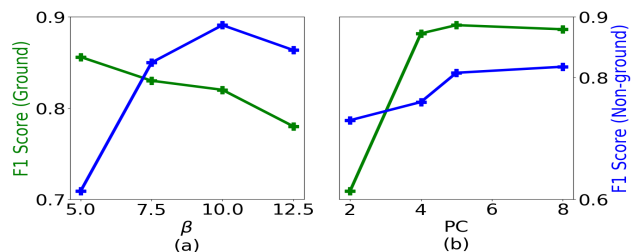


Fig. 9: The accuracy of proposed filter computed as F_1 score for separation of uninterest regions (Table. I) and interest regions (Table. II). β angle (degree) and PC are the hyperparameters that are varied one at a time while holding the other hyperparameters constant

According to the Fig. 9a, F_1 score of regions of interest is steeply increased from degree of 5 to peak of 10 degree. After that, it has a downwards trend. On the other hand, there is a dip in F_1 for region of uninterest. After 10 degrees, both F_1 scores have a decline. As shown in Fig. 9b, F_1 of region of uninterest is sharply increased from 2 to peak of 5. After that it has a steadiness. It is common for the F_1 of regions of interest as well with less score. Still, there is space to increase PC value to achieve high F_1 score. We have decided not to increase PC further because it may be a overestimation of the accuracy of the filter.

To assess the performance of the system, we ran the filter through 3000 point clouds as 3 mini batches (1000 per each). Then, we measured average running time of the proposed filter and its standard deviation per 360 degrees Velodyne-16. Result is given in Table III.

In order to compare accuracy of the proposed filter with existing methods, we have selected two other methods: fast segmentation of 3D point clouds [25] and euclidean segmentation from PCL [26]. When selecting existing methods we have not considered neural network based methods. Those are not able to run on real MAVs due to low GPU

TABLE II: Changing the PC while fixing β (10 degree) to evaluate how PC will affect on the final accuracy of the filter

PC	Region of Uninterest			regions of interest		
	P	R	F1	P	R	F1
2	0.715	0.547	0.62	0.79	0.678	0.73
4	0.917	0.7253	0.81	0.82	0.708	0.760
5	0.925	0.762	0.82	0.892	0.738	0.808
8	0.908	0.739	0.815	0.905	0.746	0.818

TABLE III: Average running time and its standard deviation per 360 degrees LiDAR scan

Nvidia Xavier ARMv8.2 @ 2.2GHz	Acer F5-573g i5-6200U @2.30 GHz
34 ms \pm 12 ms	25 ms \pm 15 ms

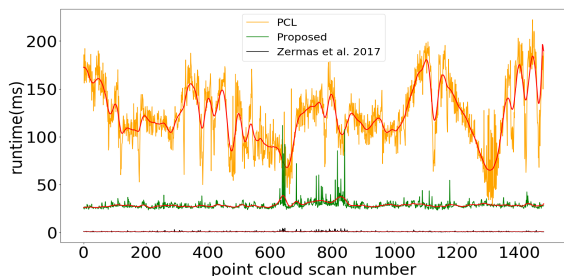


Fig. 10: Execution time approximately for 1,500 point clouds from a 16-beam Velodyne dataset with the proposed approach, Zermas’s [25] approach and euclidean segmentation from PCL [26]

capabilities. 1500 point clouds scans were processed by each of the filters. The result of the speed test is shown in Fig. 10. Runtime for euclidean segmentation from PCL was considerably higher than the proposed filter. When comparing proposed filter with Zermas [25] proposed idea, the proposed filter quite shower. This is because of finding local maxima takes more than the 50% of the total execution time per iteration.

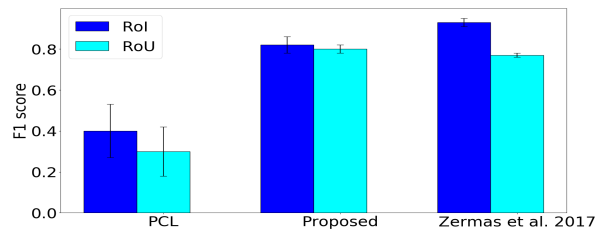


Fig. 11: RoI and ROU stand for regions of interest and region of uninterest respectively. F1 score of RoI quite higher for Zermas [25] compared to the proposed filter. On the other hand, area not interested in has slightly higher F1 score for the proposed filter

Finally, we have compared the accuracy of the proposed filter using F1 score. To calculate F1 score for the Zer-

mas’s [25] method and euclidean segmentation from PCL method, same approach which is used to find the accuracy of the proposed solution has been utilized with the same dataset. Result are shown in Fig. 11. F1 score of RoI quite higher for Zermas [25] compared to the other two methods. On the contrary, region of uninterest has slightly higher F1 score for the proposed filter compared to Zermas’s [25] method. In addition, we have more flexibility how to adjust the filter parameters based on the environment conditions where the MAV flies.

V. CONCLUSIONS

In this paper, we have presented a complete filter for segmenting regions of interest on LiDAR point cloud. The system was designed and implemented with a focus on MAVs real-time applications. Filter works on sparse LiDAR point clouds without preliminary mapping. In particular, we have presented main steps of the proposed algorithm identity locations of high densities (local maxima) within depth image, merging of original depth image with identified locations after maximizing intensities around local maxima and utilizing range angle image to search connected components in the improved depth image for segmenting out regions of interest.

Finally, we validated our approach on simulated and real conditions with a series of experiments. The accuracy and performance of the proposed filter is compared with competitive existing methods.

ACKNOWLEDGMENT

The work presented in the paper has been supported by Innopolis University, Ministry of Education and National Technological Initiative in the frame of creation Center for Technologies in Robotics and Mechatronics Components (ISC 0000000007518P240002)

REFERENCES

- [1] J. Choi, S. Ulbrich, B. Lichte, and M. Maurer, “Multi-target tracking using a 3d-lidar sensor for autonomous vehicles,” in *16th International IEEE Conference on Intelligent Transportation Systems (ITSC 2013)*. IEEE, 2013, pp. 881–886.
- [2] W. Zhang, “Lidar-based road and road-edge detection,” in *2010 IEEE Intelligent Vehicles Symposium*. IEEE, 2010, pp. 845–848.
- [3] H. Wang, B. Wang, B. Liu, X. Meng, and G. Yang, “Pedestrian recognition and tracking using 3d lidar for autonomous vehicle,” *Robotics and Autonomous Systems*, vol. 88, pp. 71–78, 2017.
- [4] B. Zhou, F. Gao, L. Wang, C. Liu, and S. Shen, “Robust and efficient quadrotor trajectory generation for fast autonomous flight,” *IEEE Robotics and Automation Letters*, vol. 4, no. 4, pp. 3529–3536, 2019.
- [5] S. Liu, M. Watterson, K. Mohta, K. Sun, S. Bhattacharya, C. J. Taylor, and V. Kumar, “Planning dynamically feasible trajectories for quadrotors using safe flight corridors in 3-d complex environments,” *IEEE Robotics and Automation Letters*, vol. 2, no. 3, pp. 1688–1695, 2017.
- [6] C. Tongtong, D. Bin, L. Daxue, Z. Bo, and L. Qixu, “3d lidar-based ground segmentation,” in *The First Asian Conference on Pattern Recognition*. IEEE, 2011, pp. 446–450.
- [7] B. Douillard, J. Underwood, N. Kuntz, V. Vlaskine, A. Quadros, P. Morton, and A. Frenkel, “On the segmentation of 3d lidar point clouds,” in *2011 IEEE International Conference on Robotics and Automation*. IEEE, 2011, pp. 2798–2805.
- [8] M. Himmelsbach, F. V. Hundelshausen, and H.-J. Wuensche, “Fast segmentation of 3d point clouds for ground vehicles,” in *2010 IEEE Intelligent Vehicles Symposium*. IEEE, 2010, pp. 560–565.

- [9] F. Moosmann, O. Pink, and C. Stiller, "Segmentation of 3d lidar data in non-flat urban environments using a local convexity criterion," in *2009 IEEE Intelligent Vehicles Symposium*. IEEE, 2009, pp. 215–220.
- [10] A. Sabirova, M. Rassabin, R. Fedorenko, and I. Afanasyev, "Ground Profile Recovery from Aerial 3D LiDAR- Based Maps," in *2019 24th Conference of Open Innovations Association (FRUCT)*, 2019, pp. 367–374.
- [11] B. Wu, A. Wan, X. Yue, and K. Keutzer, "Squeezeseg: Convolutional neural nets with recurrent crf for real-time road-object segmentation from 3d lidar point cloud," in *2018 IEEE International Conference on Robotics and Automation (ICRA)*. IEEE, 2018, pp. 1887–1893.
- [12] D. Maturana and S. Scherer, "3d convolutional neural networks for landing zone detection from lidar," in *2015 IEEE International Conference on Robotics and Automation (ICRA)*. IEEE, 2015, pp. 3471–3478.
- [13] C. Premebida, L. Garrote, A. Asvadi, A. P. Ribeiro, and U. Nunes, "High-resolution lidar-based depth mapping using bilateral filter," in *2016 IEEE 19th international conference on intelligent transportation systems (ITSC)*. IEEE, 2016, pp. 2469–2474.
- [14] T. C. Pataky, M. A. Robinson, J. Vanrenterghem, and J. H. Challis, "Smoothing can systematically bias small samples of one-dimensional biomechanical continua," *Journal of biomechanics*, vol. 82, pp. 330–336, 2019.
- [15] N. Mourad, "Ecg denoising algorithm based on group sparsity and singular spectrum analysis," *Biomedical Signal Processing and Control*, vol. 50, pp. 62–71, 2019.
- [16] G. Prathap, T. N. Kumara, and R. Ragel, "Near real-time data labeling using a depth sensor for emg based prosthetic arms," in *Proceedings of SAI Intelligent Systems Conference*. Springer, 2018, pp. 310–325.
- [17] I. Bogoslavskiy and C. Stachniss, "Efficient online segmentation for sparse 3d laser scans," *PFG–Journal of Photogrammetry, Remote Sensing and Geoinformation Science*, vol. 85, no. 1, pp. 41–52, 2017.
- [18] F. Chazal and B. Michel, "An introduction to topological data analysis: fundamental and practical aspects for data scientists," *arXiv preprint arXiv:1710.04019*, 2017.
- [19] S. Weinberger, "What is... persistent homology," *Notices of the AMS*, vol. 58, no. 1, pp. 36–39, 2011.
- [20] V. Kurlin, "A one-dimensional homologically persistent skeleton of an unstructured point cloud in any metric space," in *Computer Graphics Forum*, vol. 34, no. 5. Wiley Online Library, 2015, pp. 253–262.
- [21] C. Tomasi and R. Manduchi, "Bilateral filtering for gray and color images," in *Sixth international conference on computer vision (IEEE Cat. No. 98CH36271)*. IEEE, 1998, pp. 839–846.
- [22] H. Hassani, "Singular spectrum analysis: methodology and comparison," 2007.
- [23] N. Golyandina, V. Nekrutkin, and A. A. Zhigljavsky, *Analysis of time series structure: SSA and related techniques*. Chapman and Hall/CRC, 2001.
- [24] I. Bogoslavskiy and C. Stachniss, "Fast range image-based segmentation of sparse 3d laser scans for online operation," in *2016 IEEE/RSJ International Conference on Intelligent Robots and Systems (IROS)*. IEEE, 2016, pp. 163–169.
- [25] D. Zermas, I. Izzat, and N. Papanikolopoulos, "Fast segmentation of 3d point clouds: A paradigm on lidar data for autonomous vehicle applications," in *2017 IEEE International Conference on Robotics and Automation (ICRA)*. IEEE, 2017, pp. 5067–5073.
- [26] R. B. Rusu and S. Cousins, "3d is here: Point cloud library (pcl)," in *2011 IEEE international conference on robotics and automation*. IEEE, 2011, pp. 1–4.